Les of hydrogen-enriched methane flames in a lean-burn combustor with axial air injection

Ferrante, Gioele; Doodeman, Lennard; Rao, Arvind Gangoli; Langella, Ivan

DOI
10.1115/gt2023-103006

Publication date
2023

Document Version
Final published version

Published in
Combustion, Fuels, and Emissions

Proceedings of ASME Turbo Expo 2023
Turbomachinery Technical Conference and Exposition
GT2023
June 26-30, 2023, Boston, Massachusetts, USA

GT2023-103006

LES OF HYDROGEN-ENRICHED METHANE FLAMES IN A LEAN-BURN COMBUSTOR WITH AXIAL AIR INJECTION

Gioele Ferrante[1,†,*], Lennard Doodeman[1,†], Arvind Gangoli Rao[1], Ivan Langella[1]

[1]Faculty of Aerospace Engineering
Technical University of Delft
Delft 2629 HS, The Netherlands

ABSTRACT

Large eddy simulation (LES) paradigms are employed to analyse the internal flow field of a lean premixed swirl-stabilized combustor with axial air injection at both non-reacting and reacting conditions, for a methane and a methane-hydrogen fuel mixture. The thickened flame combustion model (TFM) with detailed chemical kinetic mechanism is employed to simulate the flow. An adaptive mesh strategy is used to maximise the mesh resolution in the flame and boundary layer regions. The numerical results for the methane flame are firstly validated against experimental velocity measurements obtained via particle image velocimetry (PIV). Subsequently the LES is employed to simulate hydrogen-enriched methane flames by keeping the same output power in the combustor, in order to obtain insights on the flow behaviour when hydrogen is added, in terms of flame stability and emissions. A POD analysis reveals the presence of a precessing vortex core (PVC) in both reacting and non-reacting conditions, and how this PVC is affected by the reactants mixture is discussed in the paper. Moreover, the flame is observed to propagate upstream in the jet core despite the use of axial air injection, although flashback is not observed. In terms of emissions, significant reduction in CO and NO_x is observed when adding the hydrogen to the reactants mixture despite the higher flame speed, the reason for are discussed in the paper.

NOMENCLATURE

PVC	Precessing Vortex Core
SGS	Sub-grid scale
TFM	Thickened flame model
AMR	Adaptive mesh refinement
AAI	Axial air injection
CRZ	Central recirculation zone
ORZ	Outer recirculation zone
POD	Proper Orthogonal Decomposition
R	Mixing tube radius [mm]
S_g	Geometric swirl number
$_{eq}$	At equilibrium
$_{air}$	Air stream
$_{fuel}$	Fuel stream
$_{ad}$	Adiabatic

†Joint first authors
*Corresponding author: g.ferrante@tudelft.nl

1. INTRODUCTION

Hydrogen is amongst the most promising clean energy carriers for powering long-distance flights due to its high energy density, zero-carbon emissions, and the possibility of producing it from water electrolysis through renewable energy [1]. Nevertheless, its relatively high flame temperature might cause substantial nitric oxides (NO_x) formation. This can be effectively decreased by using premixed lean-burn technology, and taking advantage of hydrogen's wide flammability range to stabilize the flame under very lean conditions [2]. However, due to its higher reactivity, the addition of hydrogen in existing lean-burn system imply an increase in flame speed and consequent higher risk of flashback. Furthermore, hydrogen addition affects significantly the flame dynamic response e.g. to acoustic perturbations [3]. The addition of hydrogen in such systems must thus be investigated with care to prevent unexpected flame propagation.

In lean premixed, swirl stabilised systems, flashback can occur either in the jet core, when the flame speed is higher than the reactants speed; or via the boundary layer on nearby walls; or by means of thermoacoustic instabilities; or via the so called combustion induced vortex breakdown (CIVB) [4]. Common measures to prevent the first two mechanisms consist in the increase of bulk air velocity or a decrease in swirl intensity. Nevertheless, such measures can also lead to higher pressure losses and inhomogeneous mixing, which in turn can level up emissions [5]. Alternatively, axial air injection can be employed to suppress the upstream flame propagation either in the boundary layer [6, 7] or directly in the jet core. In the latter case flashback is prevented by creating a plug flow-like axial velocity profile that pushes the

stagnation point downstream [7–9]. This type of injection was also observed to be effective in keeping low NOx levels [10]. Other works played on the axial injection of fuel rather than air to suppress flashback, although in this case NOx was observed to significantly increase [11, 12]. Despite these works, how the axial injection affects mixing and emissions is not fully clear. Moreover, mixing inhomogeneities can couple with velocity and heat release fluctuations and trigger additional instabilities or flashback [13–16]. Also, the possible presence of a precessing vortex core (PVC) may further exacerbate this coupling [13, 17, 18] and trigger flashback via the CIVB mechanisms [16]. Since hydrogen induces further inhomogeneities due to differential diffusion effects, it is of paramount importance to study the effect of hydrogen addition in combination with axial injection in order to understand, and prevent, unexpected flashback and/or increase of emissions level.

The present work aims at contributing to the development of a lean premixed hydrogen combustor for aeronautical applications with axial air injection and minimal NOx and carbon emissions. A laboratory-scale, swirl stabilised combustor located at TU Delft is numerically simulated to investigate turbulent swirling flow features, temperature field, flame stabilization and emissions. The combustor is composed of an axial swirler issuing into a mixing tube, where the fuel is injected and mixes with air before entering the combustion chamber. To prevent flashback, the stream-wise momentum component is increased by means of axial air injection [9], with the intended effect of achieving control on the stream-wise position of the flame stabilization point. Differently from the similar combustor studied in [9], where a radial swirler is used, an axial swirler is employed in the present set up. This will be used as a starting point for future parametric analysis on this design choice.

Particle image velocimetry (PIV) measurements for both reacting and non-reacting flow with a CH_4/air mixture are available to support the numerical results [19]. Large eddy simulation (LES) is used for the numerical analysis of the combustor. The capability of the LES to accurately predict unsteady reacting flow features with an affordable computational cost makes it a suitable tool to analyse the complex swirled and recirculating turbulent flow field inside the combustor as compared to Reynolds-averaged Navier Stokes (RANS) and direct numerical simulations (DNS) methodologies. Many combustion models have been proposed in the literature to mimic the interaction between turbulence, diffusion and reactions at the subgrid scale, and the reader can find a review in [20]. In the present work, this interaction is modelled using the thickened flame model (TFM), which predicts mixing in the under-resolved flame front by artificially thickening the flame [21]. The TFM is used together with detailed chemistry to properly account for the turbulence-flame interaction in presence of differential duffusion effects that can arise due to the presence of hydrogen in the fuel stream. In addition, an adaptive mesh refinement strategy based on the flame location and velocity gradients is used to maximise the mesh resolution in the flame and boundary layer regions.

The objective of this work is to shed light on the effects of hydrogen addition on the operational characteristics of lean-burn swirled combustion devices under a fixed condition of axial

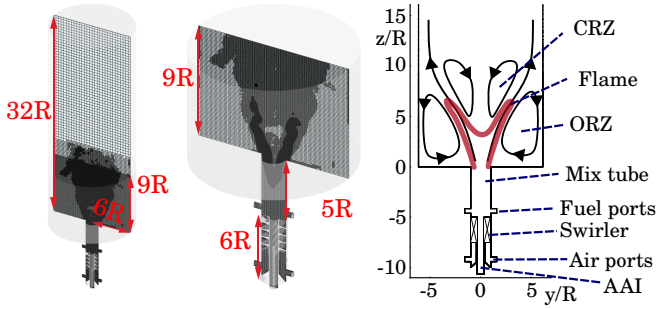

FIGURE 1: SKETCH OF THE COMBUSTOR AT TU DELFT AND TYPICAL MESH USED FOR THE LES. R IS THE RADIUS OF THE MIXING TUBE.

air injection level, and in particular to investigate the effects of hydrogen addition on flow field, flame stability, mixing effectiveness and emissions characteristics. The TU Delft combustor is operated with a minimal amount of axial air injection to prevent the occurrence of flashback. Numerical simulations of this combustor operating with CH_4 under reacting and non-reacting conditions are carried out first, and the results are compared to the experimental measurements to validate the numerical model and to provide additional insights on the general reacting flow features within the combustor and associated emissions. The analysis is then extended to another operating set point with the same power setting and air stream mass flow rate, but with a fuel mixture composed by 60% H_2 and 40% CH_4 in volume. The effect of hydrogen addition is evaluated in terms of effectiveness of fuel/oxydiser mixing, flame anchoring and emissions level as compared to the methane-only case. LES results further indicate the presence of a precessing vortex core (PVC), whose characteristics are analysed in this work by means of proper orthogonal decomposition (POD) analysis. This work is organised as follows. In Sec. 2 the laboratory scale combustor used for the present analysis is introduced. In Sec. 3 the combustion model is discussed along with further numerical details of the LES and the numerical solver. Validation and analysis of the simulation results are presented in Sec. 4. Final remarks are provided in Sec. 5.

2. TEST CASE

The laboratory-scale combustor at TU Delft [19], simulated in the present study, is illustrated in Fig. 1. The design comprises an axial swirler with a geometric swirl number $S_g = 1.1$. A mixing tube with a radius $R = 12$ mm and a length of 60 mm is present downstream of the swirler to ensure fuel/air mixing before issuing into the cylindrical combustion chamber. The total air mass flow rate $\dot{m}_{\text{air}} = 5.061$ g/s is split into a part injected axially into the mixing tube and a part entering the swirler vanes through four radial ports. The fuel is injected in the mixing tube through four separate radial ports with a diameter of 5.5 mm, which are located downstream of the swirler. The ratio between the combustion chamber and mixing tube diameter, defined as confinement ratio C, is equal to 6. The expansion of the cross section combined with the flow swirl causes a characteristic flow pattern with the formation of an outer recirculation zone (ORZ)

TABLE 1: OPERATING CONDITIONS.

Property	value	Property	value
Power [kW]	11	T_{in} [K]	288
$\dot{m}_{air}$ [g/s]	5.061	p_{out} [Pa]	101325
AAI %	5 %	S_g	1.1

and a central recirculation zone (CRZ) over which the flame stabilises as illustrated in Fig. 1. Fuel and air are at a temperature T_{in} of 288 K before entering the swirler. The combustion chamber is operated at atmospheric pressure $p = p_{out}$.

Two operating conditions are studied numerically, which differ for the fuel used: one consisting of methane-only (Case A) and one consisting of a methane/hydrogen blend (Case B), where the percentage of hydrogen amounts to 60% in volume, corresponding to 16% in mass. The fuel mass flow rate is set to $\dot{m}_{\text{fuel}} = 0.22g/s$ for the methane-only case and $\dot{m}_{\text{fuel}} = 0.18g/s$ for Case B. The reacting flow fields resulting from the methane and methane/hydrogen blends are compared at the same power output and air mass flow rates. The power output of the combustor is calculated based on the fuel mass flow rate, fuel lower heating value (LHV) and density [22], and is 11 kW. The amount of axial air injection (AAI) is defined in terms of its percentage in respect to the total air massflow rate, and is set to 5%. When hydrogen is added to the fuel, the air flow rate is kept constant. Consequently, due to the higher LHV of hydrogen as compared to methane, the equivalence ratio ϕ has to decrease to maintain the same power output of 11 kW. A summary of the overall operating conditions is given in Table 1. Fuel and oxydizer (air) compositions are instead reported in Table 2 for the two analysed cases in terms of species mass fractions Y_k.

Additional flame properties as computed from one-dimensional, freely-propagating laminar flames in the solver CHEM1D [23] with the GRI 3.0 chemical kinetics mechanism, are also reported in Table 2 for completeness. Due to the relatively low amount of hydrogen mass addition and the decreased equivalence ratio ϕ, the density of reactants, ρ_{reac}, and products, ρ_{prod}, mixtures are decreased by only 6.2% and 1% respectively when hydrogen is added (Case B). Moreover, the adiabatic flame temperature T_{ad} decreases by 1% in case B due to the combined effect of lower equivalence ratio ad higher specific heat capacity c_p in the combustion products. This implies that NOx emissions at the equilibrium (Y^{eq}_{NO} in Table 2), which are mainly generated via the thermal pathway, also decrease slightly despite the blend has a 62% higher laminar flame speed S_l and 25% thinner laminar flame thickness δ_l due to the higher reactivity of hydrogen. Carbon-based species at the equilibrium, $Y^{eq}_{\text{CO}_2}$ and Y^{eq}_{CO}, also decrease for case B, due to the reduced content of carbon in the fuel. This result is important for the analysis to be conducted in Sec. 4, as it suggests that a faster flame in the combustor does not necessary imply increased NOx when comparing at same power conditions.

Velocity measurements are available in the combustor region between the combustor entrance and an axial location of $z/R = 15$, at the aforementioned conditions. These measurements were taken using particle image velocimetry [19] (PIV) using TiO_2 seeds, a laser-pulse of 200 mJ at 532 nm and CCD cameras, and are used in this work to assess the capabilities of the LES model to predict the reacting flow physics within the combustor.

TABLE 2: REACTANTS COMPOSITION AND LAMINAR FLAME PROPERTIES FOR THE TWO TWO CASES INVESTIGATED.

Property		Case A	Case B	Δ
fuel	Y_{CH_4}	1	0.84	-16%
	Y_{H_2}	-	0.16	+16%
ϕ		0.75	0.7	-6.7%
ρ_{reac} $[kg/m^3]$		1.181	1.108	-6.2%
ρ_{prod} $[kg/m^3]$		0.177	0.175	-1.1%
T_{ad} [K]		1913	1892	-1.1%
S_l [m/s]		0.21	0.34	+38%
δ_l [mm]		0.59	0.44	-25.4%
$Y^{eq}_{\text{CO}_2}$		0.114	0.079	-30.7%
Y^{eq}_{CO}		2.07e-4	1.069e-4	-48.4%
Y^{eq}_{NO}		1.82e-5	9.46e-6	-48%
$Y^{eq}_{\text{NO}_2}$		2.68e-8	1.60e-8	-40.3%

3. LES DETAILS

The Favre-filtered Navier Stokes equations including conservation of mass, momentum and absolute specific enthalpy (sum of formation and sensible enthalpies) are solved in the LES framework. A set of Favre-filtered transport equations is solved for each chemical species involved in the combustion process within the thickened flame model approach, to be described in the next paragraph. The sub-grid scale (SGS) stresses τ_{ij} in the filtered momentum equations are closed using the one-equation, dynamic structure model, as [24]:

$$\tau_{ij} = L_{ij}\left(\frac{2k_{\text{sgs}}}{L_{ii}}\right), \tag{1}$$

where L_{ij} and L_{ii} are the Leonard stress tensor and its trace respectively, and k_{sgs} is the subgrid kinetic energy, which is modelled using a transport equation as in [16, 25]. The filtered diffusion terms in the scalar equations are modelled using a gradient hypothesis, and a subgrid Schmidt number (Prandtl number in the case of the enthalpy equation) of 0.7, except for the species, where a constant Lewis number formulation, with $Le \neq 1$, is assumed for the calculation of the diffusion coefficients. The SGS turbulence-combustion interaction model is discussed next.

3.1 Combustion model

For the present study the thickened flame model (TFM) is adopted to close the filtered reaction rate terms in the species transport equations. In this approach the flame is artificially thickened with respect to its actual size while retaining the same laminar flame speed. This is achieved by multiplying the thermal and molecular diffusivities by a factor F, and by dividing the reaction rate by the same factor [26]. The thickened flame model is adopted in conjunction with an adaptive mesh refinement strategy so that the factor F is automatically determined in order to ensure five or more cells across the flame front. Species

transport equations, including NO and NO_2, can thus be directly resolved across the thickened flame front [21], which is done here according to the multi-step kinetic mechanism GRI 3.0 [27], so that differential diffusion of hydrogen is taken into account at a resolved level. The reaction rate in each species transport equation is expressed using the Arrhenius form for both forward and reverse rate coefficients.

The flame thickening is achieved without varying the laminar flame speed using the procedure reported in [28] with dynamic local thickening. A flame sensor S is used to identify the reaction zone and ensure that the thickening factor only affects the flame region [29]. The diffusion coefficients and reaction rates are multiplied with an efficiency function to ensure that the flame propagating speed is unaffected by the flame thickening and to account for subgrid turbulence chemistry interaction, e.g. flame wrinkling [26]. The transport equation for the mass fraction Y_i of species i, in Einstein's notation, is then written as

$$\frac{\partial \rho Y_i}{\partial t} + \frac{\partial \rho Y_i u_j}{\partial x_j} = \frac{\partial}{\partial x_j}\left(\rho \cdot E \cdot F \cdot D_i \frac{\partial Y_i}{\partial x_j}\right) + \frac{E}{F}\dot{\omega}_i \qquad (2)$$

where ω_i is the reaction rate per unit volume, ρ is the mixture density and u_j is the velocity component in direction j. The diffusivity coefficient D_i is pre-multiplied by $E \cdot F$ to counteract the effect of the decreased flame wrinkling.

The thickening local factor F is modelled as $F = 1+(F_{max}-1)S$. The maximum value of F can be imposed as a function of the desired number of cells in the flame front n_{res}, the local cell size Δ, and the flame thickness δ_l, so that $F_{\max} = n_{res}\Delta/\delta_l$. The flame sensor S is computed as

$$S = \max\left[\min\left(\beta \frac{|\overline{\dot{\omega}}_{\text{sens}}|}{\dot{\Omega}_{\text{sens},0}(\phi)} - 1, 1\right), 0\right] \qquad (3)$$

where $|\overline{\dot{\omega}}_{\text{sens}}|$ is chosen to be the methane reaction rate for all simulations in the present work, $\Omega_{\text{sens},0}(\phi)$ is the maximum reaction rate in a premixed laminar flame at a given equivalence ratio ϕ, and β is a modelling coefficient.

The efficiency function measures the reduction in the subgrid flame surface due to the thickening process and is defined as the ratio between the wrinkling parameter for unthickened and thickened flames, $E = \Xi|_{\delta=\delta_l}/\Xi|_{\delta=F\delta_l}$. The wrinkling parameter Ξ_Δ in the latter is modelled as

$$\Xi_\Delta = \left(1 + \min\left[\frac{\Delta}{\delta_l} - 1, \Gamma_\Delta\left(\frac{\Delta}{\delta_l}, \frac{u'_\Delta}{s_l}, Re_\Delta\right)\frac{u'_\Delta}{S_l}\right]\right)^\beta \qquad (4)$$

where u'_Δ is the subgrid scale velocity, S_l is the laminar flame speed, Δ is the LES filter size (taken as the cubic root of the local cell volume), and β is a dynamically-modelled exponential coefficient [30]. The factor Γ_Δ accounts for the strain effect in the flame caused by the sub-grid turbulent scales and is calculated based on the Reynolds number Re_Δ, the turbulence fluctuations u'_Δ and flame characteristics [28]. Further details on this model can be found in [21, 28].

3.2 Numerical details

The LES equations are resolved using the pressure-implicit with splitting of operators (PISO) algorithm for the pressure-velocity coupling [31] available in the commercial software ConvergeCFD [32]. A minimum of 2 and a maximum of 9 iterations are used to solve the velocity and pressure fields through predictor-corrector strategy. An external loop is used to solve for the energy, species and other transport equations. A variable time step is used to guarantee a CFL number smaller than 0.5 everywhere in the domain. The temporal terms are discretised using an implicit Euler scheme, while second order central schemes are used for all the convective terms except for the subgrid kinetic energy transport equation, where an upwind scheme is used. No blended scheme or limiters are used.

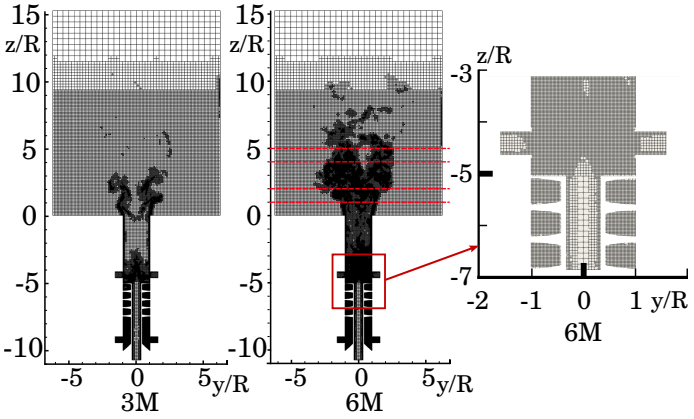

FIGURE 2: MIDPLANE RENDERING OF THE MESHES USED FOR THE LES WITH UPPER RESOLUTION OF 3M (LEFT), 6M (CENTRE) AND 12M (RIGHT) CELLS. DASHED LINES INDICATE THE LOCATIONS WHERE MEASUREMENTS ARE TAKEN.

Boundary conditions are assigned as follows. A flat velocity profile is specified at the inlets according to the respective mass flow rate from the experimental data, while a zero-gradient condition is given at the outlet. At the walls the boundary layer is not entirely resolved within the computational grid, therefore wall functions are used along with the non-slip condition. Both the Werner and Wengle model [33] and the Law of the Wall model [34] were tested in preliminary simulations for sensitivity purposes, showing similar results. The former is computationally more efficient and is therefore used in this work. Temperature is assigned at the inlet using data from the experiments, and adiabatic conditions are assumed at the walls. All scalars are zero at the inlet except for oxygen, nitrogen and fuel, which are specified according to the specific fuel and air compositions. A zero-gradient condition is used for all scalars at the outlet and on walls, except for the subgrid kinetic energy, which is zero at the walls.

The mesh has been setup using the adaptive mesh refinement utility available in ConvergeCFD. A baseline mesh with a characteristic cell size of 5 mm in all directions is used for initialisation purposes. Subsequently, the mesh is refined based on sub-grid scale (SGS) velocity, wall distance values and the TFM thickening factor. Three mesh resolutions have been tested for sensitivity purposes, where the total number of cells is limited respectively to 3M, 6M and 12M cells. For the 6M mesh, also used for follow-up analyses, the maximum cell size results in 0.3 mm in the flame front and 1.25 mm in the region nearby

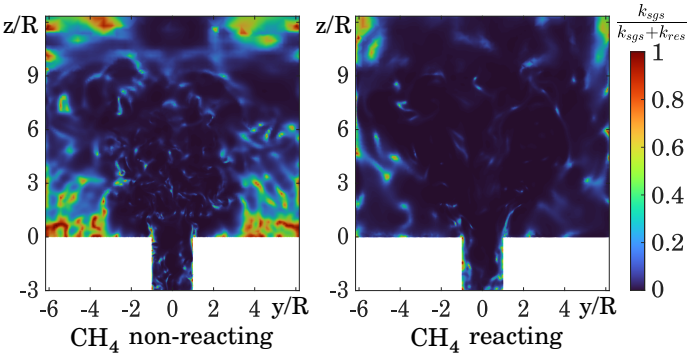

FIGURE 3: POPE'S CRITERION OF TURBULENT KINETIC ENERGY [35] IN THE MIDPLANE OF THE COMBUSTOR.

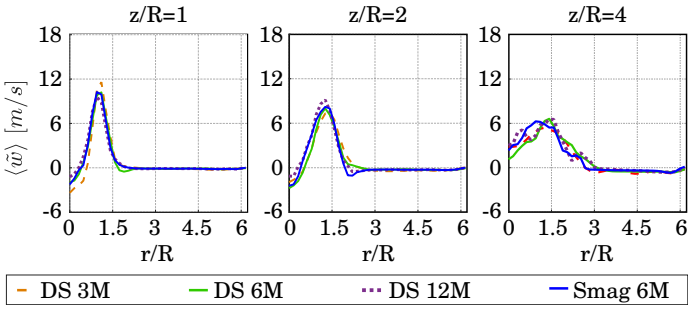

FIGURE 4: RADIAL PROFILES OF MEAN AXIAL VELOCITY AT DIFFERENT STREAMWISE LOCATIONS OBTAINED FROM NON-REACTING METHANE/AIR LES, FOR DIFFERENT MESH SIZE AND TWO TURBULENCE MODELS: DYNAMIC STRUCTURE MODEL (DS) AND SMAGORINSKY MODEL (SMAG).

(up to a downstream location of $9R$ in the combustion chamber). At the wall, the height of the first cell is limited to a maximum $y^+ = 15$, where $y^+ = yu_\tau/\nu$ is the normalised wall distance, y is the wall-normal coordinate, u_τ is the friction velocity and ν is the kinematic viscosity. The typical mesh in the combustor midplane at a generic time step is shown in Fig. 2 for the three resolutions, where it can be appreciated how the mesh resolution increases near the walls and in the regions where the flame front is expected. Pope's 80% turbulent kinetic energy criterion [35] is used to evaluate the mesh quality in preliminary simulations, and it is shown in Fig. 3 (only for the 6M mesh). As observed from the figure, the ratio between modelled, k_{sgs}, and total turbulent kinetic energy (resolved plus SGS) is observed to be smaller than 0.2 [35] everywhere except in the low-speed, ORZ region near the walls (non-reacting case), where both resolved and SGS turbulent kinetic energy go to zero, and downstream the region of interest, where the mesh coarsens.

Each simulation is run fora total period of 15 flow-through times, where the flow-through time $t_{\text{flow}} \approx 10$ ms is defined as the time a parcel of fluid needs travelling at the bulk speed $U_b \approx 10$ m/s to reach the position $z = 110$ mm ($\sim 9R$). Six flow-through times are used in each simulation to pass the transient (after ignition in the reacting flow cases) and further nine to collect the statistics. The achievement of the steady state after transient was verified by monitoring the fluctuations of massflow rate at the section $z = 9R$. All simulations were run on the TU Delft HPC12 internal cluster using 480 cores in parallel. This resulted in about $1.9 \cdot 10^5$ CPU hours per simulation using 2.3 GHz AMD processors.

4. RESULTS AND DISCUSSION

4.1 Sensitivity analysis & validation

A preliminary analysis using different turbulence models and mesh sizes is carried out first for the non-reacting case with the CH_4/air mixture. Time averaged axial velocity $\langle\tilde{w}\rangle$ radial profiles are shown in Fig. 4 for different stream-wise locations z in the combustor, with $z = 0$ corresponding to the outlet of the mixing tube; and compared with the experimental measurements in [19]. Two SGS turbulence models are compared on the 6M mesh: the dynamic structure model (DS) [24] and the Smagorinsky model (Smag) [36]. As observed, the predicted velocity field does not exhibit a strong dependence on the chosen mesh. Thus, the 6M elements mesh is retained for the following analysis, as this mesh satisfies Pope's criterion as was shown in Fig. 3. Results obtained with the two turbulence models are also very similar, with a relative error of the peak velocity that remains below 3% at any axial location. Since the dynamic structure model is suited for anisotropic turbulence effects [24] that may arise in the reacting case, the latter is retained from now on for the following analyses.

Next, radial profiles of mean axial velocity $\langle\tilde{w}\rangle$ are compared to experimental findings [19] at four axial locations in Fig. 5 for both non-reacting and reacting cases. Only the Case A of Table 2 (methane-only fuel) is shown as no experimental data is available for the methane/hydrogen blend case. It is worth to mention that the following comparison is only performed to gain an understanding of the general flow features within the combustor and the ability of the LES to capture these from a qualitative point of view. In particular, significant backflow was observed at the combustor outlet for the non-reacting case during the experimental campaign, with consequent uncertainty in the outlet velocity and pressure boundary conditions, that could not therefore be exactly assigned in the LES. These, in turn, were observed to affect the jet spread angle at the entrance of the combustor, which is larger in the experiments with consequent shorter central recirculation region. Adiabatic boundary conditions at the wall might also have influenced the jet spread angle [37] as compared to real conditions, although this effect is expect to be limited in the non-reacting case. In general, the effect of the imposed boundary condition on the calculated flow field can be minimized by appropriate modifications in the computational domain geometry, e.g. by elongating the combustion chamber or including part of the external atmosphere in the computational domain [38]. While this strategy works well for reacting flows issuing in atmosphere, it is unfortunately not applicable to the present case, because an exhaust tube is mounted at the outlet of the experimental set up, making it hard to identify an outlet location of known pressure conditions. It is also worth noting that the spread angle was observed to remain unaffected in the LES sensitivity analysis discussed earlier, using different mesh resolutions and SGS models, and also repeating the simulation with a different code (OpenFOAM) and similar numerical details, which suggests that

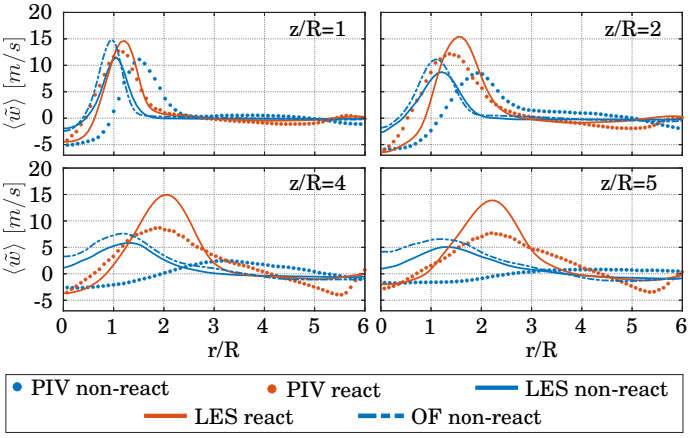

FIGURE 5: RADIAL PROFILES OF MEAN AXIAL VELOCITY FROM LES AND EXPERIMENTS, FOR THE REACTING AND NON-REACTING METHANE-ONLY CASES.

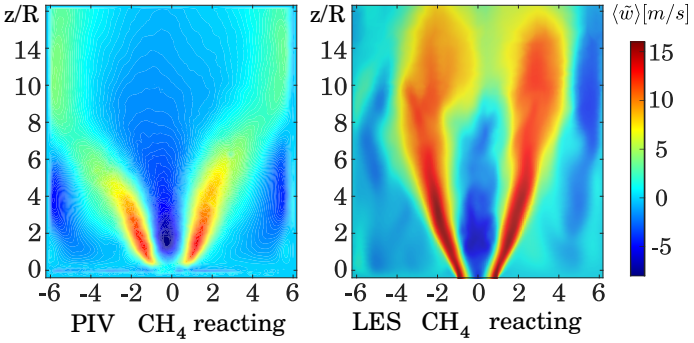

FIGURE 6: MIDPLANE CONTOURS OF AXIAL VELOCITY FROM EXPERIMENTS (LEFT) AND LES (RIGHT).

numerical diffusion or modelling may not be the cause of these differences. Therefore, comparisons of statistics between LES and PIV measurements for the non-reacting case would not be meaningful and are not performed here. On the other hand, non-reacting LES results are still presented in light of the comparisons between reacting and non-reacting conditions and their relative differences to be discussed in the next sections.

The backflow effect on the spreading angle was somewhat observed to be less strong in the reacting case, probably due to the flow acceleration as result of the gas expansion in the flame region. A comparison of midplane contours of axial velocity between LES and experiments is shown in Fig. 6. As can be observed, the jet spread angle and velocity field from the LES remains similar to that observed in the experiment in the region of the flame (up to $z/R = 5$), while significant deviations are observed in the region downstream, where the measured flow field indicates negative axial velocity along the centreline up to at least $z/R = 16$. The extent of the region with negative velocity could be varied in the LES by varying the outlet boundary conditions (not shown). Considering that finding these exact conditions is quite a tedious operation, and since only the flame region is of interest here, statistics are compared next only up to $z/R = 5$ as for the present work the only purpose of these comparisons is to get a qualitative understanding of the LES ability in predicting a meaningful reacting flow field. Boundary conditions at the outlet in the LES are thus kept as indicated in Section 3.2.

Radial profiles of mean axial velocity as predicted from the LES are compared to experimental values in Fig. 5 at different axial locations within the flame region. The velocity field as predicted by the LES for the reacting case (methane-only) is observed to mimic the experimental trend quite well at $z/R = 1$. Some overestimation is observed at more downstream locations, which is partly explained by the approaching backflow region in the experiments, and could in part be explained by heat losses at the wall, e.g. see [39], which were not taken into account in the LES. However, the location of the peaks is well predicted, which suggests that the flame shape in the LES and in the experiments is similar. The location of these peaks appear to shift towards higher radial locations in the reacting case as compared to the non-reacting case, also shown in the figure, which indicates a larger jet spreading angle at the combustor entrance, with consequent larger extent of the central recirculating region (Fig. 6). This variation is also observed qualitatively in the experiments, whose non-reacting condition is only shown here for reference since, as mentioned earlier, values are not directly comparable to those of the LES. Note that the numerical data for the non-reacting case obtained using OpenFOAM are also shown for reference.

The above analysis indicates that the LES model used in the present work predicts the velocity field with reasonable accuracy, at least in the flame region. Since velocity gradients increase due to the heat release from the flame, these comparisons further suggest that the correct flame shape and position might have been captured, although quantitative investigations on temperature and species are necessary to validate this assessment, and they could not be performed as this data was not available from experiments. Because of the above reasons, the LES setup with TFM and detailed chemistry is further used for the investigations in the next section.

4.2 POD Analysis and PVC

The proper orthogonal decomposition (POD) method is employed to identify the presence of coherent fluctuating structures and describe their behaviour. This anlysis is further finalised to investigate the possible presence of a precessing vortex core (PVC) in the flow, since this unsteady structure can often form in confined swirled flows [17] and interact with the flame dynamics. The reacting LES dataset is therefore analysed with the method of the snapshots described in [40]. The same analysis is performed on the non-reacting, methane-only LES dataset, and results are compared to those obtained from PIV [19]. According to the POD method, the fluctuating velocity field in the transversal direction y, $v'(\mathbf{x}, t)$, can be described as a linear combination of a set of orthonormal spatial functions (POD modes) $\mathbf{\Phi}_k(\mathbf{x})$, weighted by time-varying coefficients $a_k(t)$:

$$v(\mathbf{x}, t) = \sum_{k=1}^{\infty} a_k(t)\mathbf{\Phi}_k(\mathbf{x}) \tag{5}$$

The first n POD modes capture most of the turbulent kinetic energy (TKE) of the fluctuating flow field (only including the in-plane fluctuations). These modes give information about the

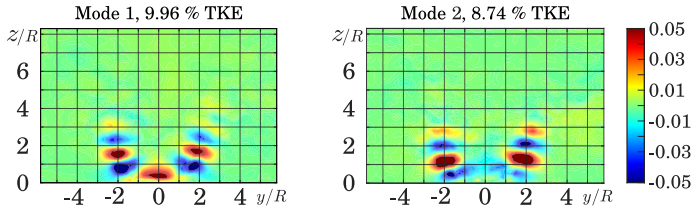

FIGURE 7: FIRST TWO POD MODES COMPUTED FROM THE EXPERIMENTAL DATASET FOR THE NON-REACTING, METHANE-ONLY CASE.

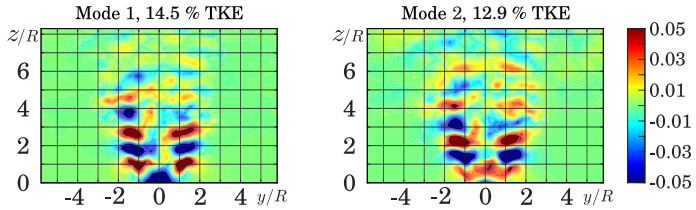

FIGURE 8: FIRST TWO POD MODES COMPUTED FROM LES FOR THE NON-REACTING, METHANE-ONLY CASE.

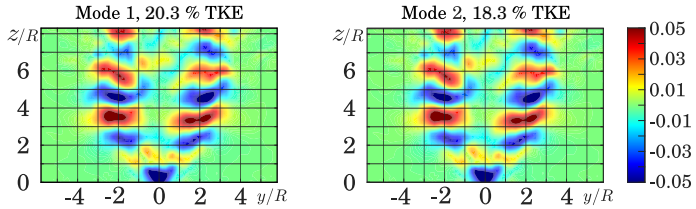

FIGURE 9: FIRST TWO POD MODES COMPUTED FROM LES FOR THE REACTING, METHANE-ONLY CASE.

degree of correlation between the velocity fluctuation v' at each point of the domain and it is possible to relate them to the coherent structures in the fluctuating flow field. The POD modes are obtained by computing the n eigenvectors $\mathbf{\Phi}$ of the correlation matrix ($\mathbf{C_s}$), defined as:

$$\mathbf{C_s} = \frac{1}{m-1}\mathbf{V}\mathbf{V}^T, \tag{6}$$

where each of the m rows of the matrix $\mathbf{V}$ contain the v' values at the n domain points at a specific time step. The corresponding eigenvalues indicate the contribution of each mode to the TKE on the plane associated with fluctuations in the transversal direction y, and most of the fluctuations can be described by the first two modes. The temporal coefficients $a_k(t)$ are computed as the projection of the velocity matrix on the modes, and by looking at their evolution in time it is possible to identify whether the associated mode exhibits an oscillatory behaviour. The POD analysis performed on the PIV data used a total of 200 snapshots at an acquisition frequency of 15 Hz. Since the PVC has a higher frequency, no assessment is possible on the frequency from the PIV data, but only on the coherence of the two POD modes. On the contrary, the acquisition frequency in the LES is about 50 kHz, and a time window of 8 to 14 ms was used to process the POD data, corresponding to at least one PVC revolution.

POD modes obtained from the LES for the methane-only cases (reacting and non-reacting) are firstly compared to those obtained using the experimental dataset to assess whether a similar dynamics is predicted. The first two spatial modes obtained using the PIV dataset are plotted in Fig. 7, which contribute respectively to 9.96% and 8.74% of TKE on the 2D plane. Since regions with similar values of the spatial mode $\mathbf{\Phi_k}(\mathbf{x})$ correspond to in-phase fluctuations of v' (counter-phase if of opposite sign), these plots reveal the presence of transversal oscillations and the shedding of vortical structures. In particular, the pattern of the first two modes near the inner shear layer reveals the presence of the typical helical structure associated with the PVC [41, 42]. In fact, the 90° phase shift in the streamwise location of the two modes is associated to the motion of the PVC and describes the periodic movement downstream of the helical vortical structure intersecting the plane [43]. These modes are compared to those obtained from the LES next. Figure 8 shows the first two POD modes from the simulated non-reacting case. It can be observed that modes 1 and 2 from the LES also present the characteristic pattern associated with the presence of the PVC described before. These two modes together contribute to about 27.4% of the TKE on the 2D plane, which is higher than the amount obtained summing the first two modes from the PIV, but consistent with past works on swirled configurations at similar conditions [41]. The analysis of the temporal coefficients associated with these modes further reveals a frequency of precession of about 250 Hz, which is consistent with values reported in literature [41]. Note that the distribution of these spatial modes is different between LES and PIV as it reflects the different jet spreading angle discussed earlier.

The reacting case is analysed next using the LES dataset. The first two POD modes are shown in Fig. 9 for the methane-only case. An inspection of these modes indicates that the PVC is still present in the flow when combustion occurs, which is in contrast to findings for similar configurations (e.g. see [41]). Moreover, both modes appear to contribute to the TKE in higher percentage as compared to the non-reacting case, suggesting that the intensity of the PVC has also increased. The addition of hydrogen to the flow is also investigated for completeness, and related POD modes are shown in Fig. 10. It is important to note, however, that only about 5 ms time-window was used for this case due to computational limitations, since POD data was not originally stored and further simulation time had to be allocated to extract this data. Although 5 ms is sufficient to capture an entire PVC revolution (see discussion later on temporal coefficients), the reader is reminded to interpret these results with care. As can be observed in the figure, when hydrogen is added to the fuel, the amplitude of the modes associated to the PVC tend to be much milder near the combustor entrance, which may be a consequence of the stronger reactivity of hydrogen. This behaviour might indicate a suppression of the two modes near the combustor entrance or, alternatively, one can interpret it with a delayed development of the helicoidal structure of the PVC and the consequent shift downstream of the oscillatory region in respect to the flame anchoring position (which has moved upstream, see Fig. 12).

The temporal coefficients associated with the POD modes and their respective spectra are further shown in Fig. 11. The analysis of the respsective spectra indicates that the PVC fre-

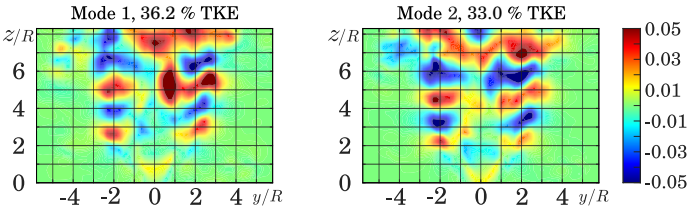

FIGURE 10: FIRST TWO POD MODES COMPUTED FROM LES FOR THE REACTING, METHANE/HYDROGEN BLEND CASE.

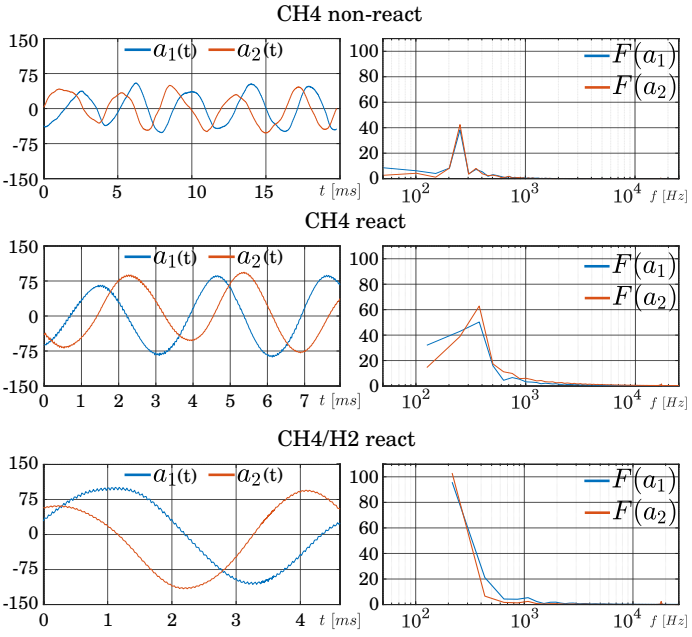

FIGURE 11: TEMPORAL EVOLUTION OF THE COEFFICIENTS ASSOCIATED TO THE FIRST TWO POD MODES (LEFT) AND THEIR SPECTRA (RIGHT), OBTAINED FOR NON-REACTING AND REACTING (METHANE ONLY AND HYDROGEN BLEND) CASES.

quency has increased from about 250 Hz in the non-reacting case to about 380 Hz in the methane-only reacting case. For the hydrogen blend case, the frequency of the temporal mode seem to decrease below 220 Hz, although the time window used here may not be sufficient, as explained earlier, to have a precise assessment of this frequency. The Nyquist criterion remains satisfied. By looking at the temporal evolution of the coefficients, one can however still appreciate that the frequency associated to the PVC revolution is somewhat decreased by the hydrogen addition, and that at least one PVC revolution was captured within the time window used for the POD.

These differences are interesting as they might explain some non-straightforward behaviour observed in the flow field when hydrogen is added to the flow, which is discussed in the next section.

4.3 Effects of hydrogen addition to flame and emissions

The effects of H_2 addition to the fuel stream are investigated in this section. The most obvious effect of adding hydrogen is that the flame propagates and stabilises upstream in the mixing tube, which can be appreciated by looking at the midplane temperature

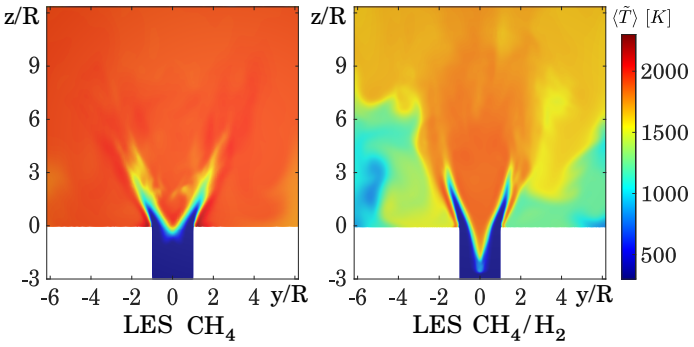

FIGURE 12: MIDPLANE CONTOURS OF MEAN TEMPERATURE FROM LES FOR METHANE-ONLY AND METHANE/HYDROGEN CASES.

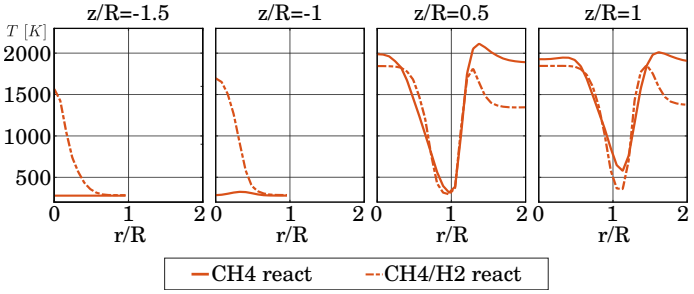

FIGURE 13: RADIAL PROFILES OF MEAN TEMPERATURE AT DIFFERENT AXIAL LOCATIONS, OBTAINED FROM LES FOR METHANE-ONLY AND METHANE/HYDROGEN CASES.

contours in Fig. 12. In particular, the averaged anchoring point of the flame along the centreline moves from a location of about $z/R = 0$ (combustor entrance) to $z/R \approx -2.5$. This also implies a central recirculation zone that extends within the mixing tube. The higher flame speed, however, does not correspond to a higher temperature as observed in the figure, which is consistent with the adiabatic flame temperatures computed from the flamelets (see Table 2). These lower temperatures in the hydrogen blend case are mainly driven by the overall leaner mixture in this case. Moreover, temperature in the ORZ in the case of the blend suggests that combustion is incomplete there and mixing is less efficient. The non-perfectly symmetric temperature field observed in the ORZ may further be the result of a higher residence time at this location, which might be associated to the lower PVC frequencies observed in the temporal modes in Sec. 4.2. Further analyses on this aspect are beyond the scope of this work and will pe performed in future studies.

Radial profiles of mean temperature for the two reacting cases are shown in Fig. 13 in the region immediately upstream and downstream the combustor entrance. These indicate that while temperature in the hydrogen blend case is much higher in the mixing tube due to the presence of the flame, immediately downstream the combustor entrance the temperature behaves similarly, except within the ORZ as mentioned before. It is also interesting to note that the bubble of recirculating burnt gases in the hydrogen blend case acts now as an obstruction in the mixing tube, reducing the effective cross-sectional area at the exit of the mixing tube. This results in slightly higher velocities near the

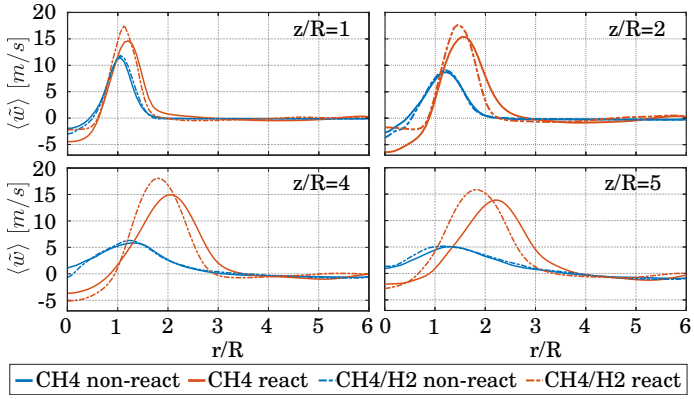

FIGURE 14: RADIAL PROFILES OF MEAN AXIAL VELOCITY AT DIFFERENT AXIAL LOCATIONS, OBTAINED FROM LES FOR THE METHANE-ONLY AND METHANE/HYDROGEN CASES.

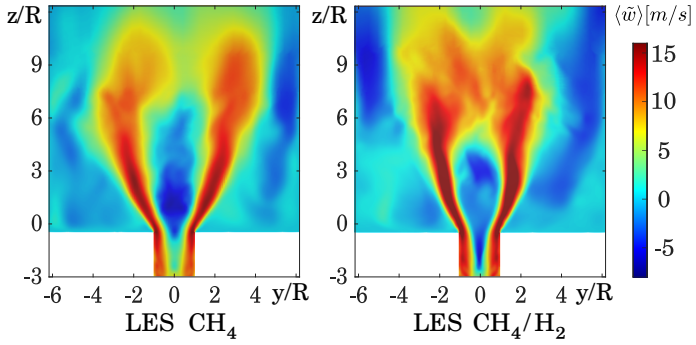

FIGURE 15: MIDPLANE CONTOURS OF AXIAL VELOCITY OBTAINED FROM LES FOR THE REACTING CONDITION WITH METHANE-ONLY AND METHANE/HYDROGEN FUEL.

combustor entrance in the case of the hydrogen blend, as can be observed in Fig. 14, and a lower spreading jet angle (with consequent shorter extension of the central recirculation region in the combustor), as shown in Fig. 15. These differences further affect the effective swirl number and fuel/oxidiser mixing process in the mixing tube, which are discussed next. It is worth to note that the addition of hydrogen in the non-reacting case (Fig. 14) does not result in any significant effects on jet spreading, size of the recirculation zones and velocity field, since the variation in the reactants mixture density is minimal (see Table 2).

The evolution of the effective swirl number S_w, averaged equivalence ratio ϕ, and its standard deviation σ throughout the mixing tube are shown in Fig. 16 to gain further information on the flow field behavior within the mixing tube and how this can affect the combustion downstream. These quantities are in fact significantly affected by the propagation of the flame within the mixing tube as one would expect. The effective swirl number is computed in the LES as the ratio between the axial fluxes of tangential and axial momentum [44]:

$$S_w = \frac{\int \overline{\rho}\widetilde{w}\widetilde{u}_\theta r dA}{R\int \overline{\rho}\widetilde{w}^2 dA} \tag{7}$$

where $\overline{\rho}$ is the filtered density of the local mixture, u_θ is the velocity component in the azimuthal direction, r is the radial co-

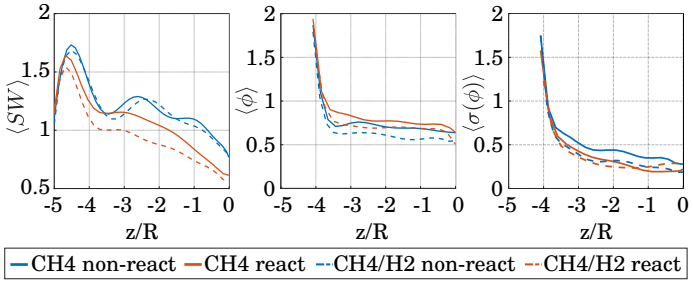

FIGURE 16: AXIAL PROFILES OF MEAN SWIRL NUMBER (LEFT), EQUIVALENCE RATIO (CENTRE) AND ITS STANDARD DEVIATION (RIGHT) IN THE MIXING TUBE AHEAD OF THE COMBUSTOR CHAMBER.

ordinate and A is the sectional area in the mixing tube. At the outlet of the swirler vanes S_w equals the geometric swirl number $S_g = 1.1$. As observed from Fig. 16, the effective swirl number then increases in the mixing tube first up to $z/R \approx -5.5$, to then decrease again quickly at $z/R \approx -4.5$. This decrease is due the reduction of irregularities in the radial and tangential directions as the flow evolves in the mixing tube, consistently to previous studies [45], and is aided by the fuel injection between $z/R = -4.1$ and $z/R = -4.6$. In turn, this affects the viscous dissipation and radial flow divergence, thus the axial flux of angular momentum [46]. The resulting effective swirl number at the end of the mixing tube is about 0.77 for both the non-reacting cases regardless of the fuel, while it decreases to 0.61 and 0.57 in the reacting cases respectively for the CH_4-only and the CH_4/H_2 blend. This decrease as compared to the non-reacting case is caused by the increased axial velocity at the combustor entrance [46], and is thus of larger extent in the hydrogen blend case consistently with the higher axial velocity observed in Fig. 14. The slightly higher effective swirl number in the the reacting methane-only case may also partly explain the wider opening of the jet observed in Fig. 14 as compared to the CH_4/H_2 case [47]. More interestingly, the evolution of the effective swirl number in the mixing tube between the swirler vanes exit and the combustor entrance is different in the hydrogen blend case, exhibiting lower values, which is likely to be a consequence of the flame being located in the mixing tube. These differences could affect the mixedness of the flow, causing variation of equivalence ratio up to the flame region with a direct effect on the emissions [9, 48]. The level of unmixedness in the flame region is therefore investigated using the method of Li et al. [49] as follows. By looking at the mean behaviour of equivalence ratio ϕ and its standard deviation σ in Fig. 16, one can notice that, while the mixture becomes substantially leaner when hydrogen is added to the mixture, no significant change occurs in terms of σ. This might suggest that any change in emissions has to be attributed to variation in mean equivalence ratio, rather than turbulent mixing or further fluctuations caused by differential diffusion effects. The distribution of mean equivalence ratio near the flame anchoring point is thus further investigated by looking at the radial profiles of ϕ at different axial locations in Fig. 17, for both reacting and non-reacting conditions. First, one can notice that there is significant variation of ϕ in the radial direction for all conditions investigated in this

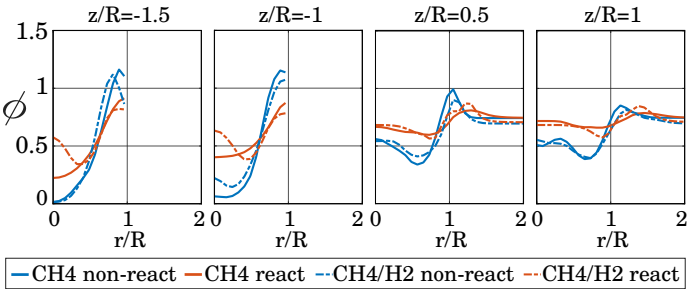

FIGURE 17: RADIAL PROFILES OF AZIMUTHALLY AVERAGED EQUIVALENCE RATIO AT DIFFERENT AXIAL LOCATIONS AT THE END OF MIXING TUBE AND AT THE BOTTOM OF THE COMBUSTION CHAMBER (FLAME REGION)

work, and at all axial locations. This is the result of the fact that the fuel is injected radially in the highly turbulent swirling flow in the outermost region of the mixing tube (at an axial coordinate of $z/R = -4.1$) and has to mix into the mixing tube core, where the stream of axial air injection implies $\phi = 0$. It is worth mentioning that the momentum of the injected fuel in the transversal direction is small compared to the axial momentum of the swirling air and the axial air streams. For this reason, mixing near the centreline occurs mainly through turbulent and molecular diffusion, rather than convective processes. Moreover, for all conditions the reactant mixture does not achieve perfect homogeneity at the entrance of the combustor chamber ($z/R = 0$), although mixing is observed to significantly improve in the reacting cases. Similarly to earlier observations, the non-reacting cases exhibit very similar mixing behaviours and no significant differences are observed in equivalence ratio at almost all location. Let's note that, since the global equivalence ratio in the case of the hydrogen blend is lower than in the methane-only case (the two cases are compared at the same output power), the value of the peaks must also be lower as observed in Fig. 17 (see for example $z/R = -1.5$). Nevertheless, despite the milder equivalence ratio radial gradients driving turbulent and molecular diffusion, the centreline appears to get richer at a faster rate in the case of the hydrogen blend even in the non reacting case, which becomes evident at $z/R = -1$ near the centreline. This effect, which is due to the higher diffusivity of hydrogen that improves the air/fuel mixing, becomes milder downstream because convective effects in the recirculation zone become dominant. Although this variation of equivalence ratio distribution right upstream the combustor entrance ($z/R = 0$) did not lead to any significant differences in the flow field behaviour in the non-reacting case, it may trigger an upstream propagation of the flame in the reacting case. For the reacting cases, the presence of the flame appears to improve mixing near the combustor entrance, especially in the CH_4/H_2 case where both flame and recirculation bubble have moved upstream. The recirculation brings in fact more homogeneous mixture parcels from the combustion chamber to inside the mixing tube. On the other hand, the significant increase in equivalence ratio near the centreline at $z/R = -1$ is still observed for the reacting case in the case of the hydrogen blend, as compared to the methane-only case. By comparing the profiles of ϕ with the temperature profiles in Fig. 13, one can thus argue that the upstream propagation of the flame near the centreline in the hydrogen blend case is partly due to the equivalence ratio being locally higher than expected (implying higher flame speeds) as compared to the methane-only case. Another observation is that the flame in downstream positions burns over a wider range of equivalence ratios in the hydrogen blend case, as compared to the methane-only case. These local differences in mixing are expected to affect the level of emissions, which are discussed next.

In Table 3, the sectional average of mean mass fraction of CO_2, CO and NOx (NO and NO_2) at the combustor exit plane are provided. The addition of hydrogen to the fuel results in a decrease in CO_2 and CO, as one would expect for a fuel mixture containing fewer carbon atoms and an overall decrease of equivalence ratio. Moreover, consistently with the decrease of temperature peaks in the mean field, an overall decrease of 88% of NO is observed. Similarly, the mass fraction of NO_2 is observed to decrease of about 30%. The emission values from the LES and their decrease appear to be in line with the 1D laminar calculations in Table 2. However, the emissions from the LES are in general higher than in the laminar case due to turbulence-chemistry interaction effects and the presence of equivalence ratios inhomogeneities as described before. In fact, the presence of rich regions (outer part of the mixing tube) intuitively causes local increase in carbon based emissions and produces overshoots of temperature which favour the NO formation. Moreover, due to its slow rate of formation (nitrogen oxydation), the production of NO is highly affected by flow features such as recirculation zone and turbulence, which ultimately affect the residence time. These results indicate the paramount importance of achieving an effective mixing to have a balance between emissions and flame position in the context of lean swirled combustor technology. On the other hand, the relative strong decrease of NO in the hydrogen blend case as compared to the methane-only case could also be a result of a decreased flame wrinkling observed for the former, which in turn is a result of the higher local reactivity of the hydrogen blend. In fact, the flame regime is observed to shift towards the bottom-left part of the Borghi diagram in the case of the hydrogen blend, as observed in Fig. 18, which indicates weaker turbulent fluctuations on the flame. This results in less overshoots of temperature, which can be verified by looking at the temperature variance in the region of the flame in Fig. 19, except for $z/R = -1$ since a flame is not present in the methane-only case at this location. The smaller variance of temperature implies less peaks of temperature and, given the exponential dependence of thermal NOx on temperaure,

TABLE 3: SECTION-AVERAGED MEAN MASS FRACTIONS OF CARBON-BASED SPECIES AND NOX FROM LES AT THE COMBUSTOR EXIT FOR METHANE-ONLY AND METHANE-HYDROGEN CASES.

Species	CH_4	CH_4/H_2	ΔY
$\langle\widetilde{Y}_{CO_2}\rangle$	0.12	0.08	-33 %
$\langle\widetilde{Y}_{CO}\rangle$	2.21e-4	2.55e-5	-88 %
$\langle\widetilde{Y}_{NO}\rangle$	5.08e-5	1.41e-5	-72 %
$\langle\widetilde{Y}_{NO_2}\rangle$	7.62e-8	5.32e-8	-30 %

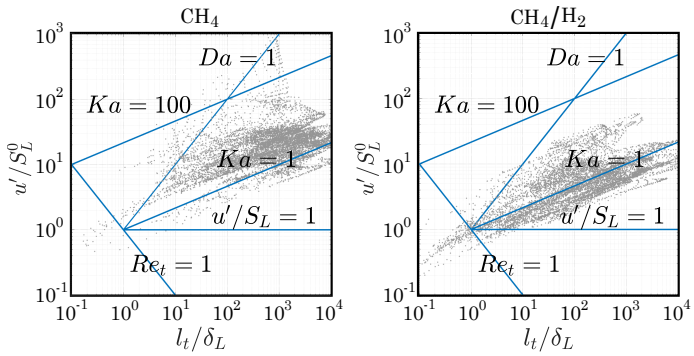

FIGURE 18: PREMIXED REGIME DIAGRAM WITH SCATTER ON TOP OF THE LOCAL FLAME CONDITION FOR THE METHANE-ONLY (LEFT) AND HYDROGEN BLEND (RIGHT) CASES.

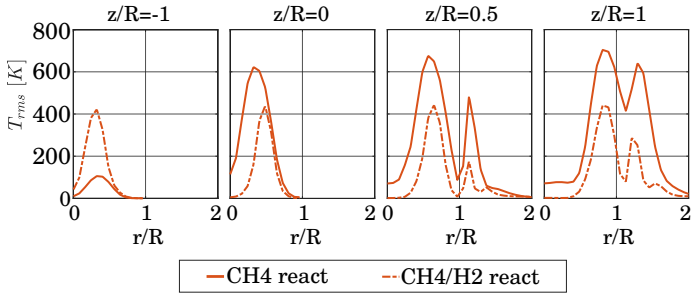

FIGURE 19: RADIAL PROFILES OF TEMPERATURE RMS IN THE REGION OF THE FLAME BRUSH (ABOUT $-1 \leq z/R \leq 1$) FOR THE REACTING CASES PREDICTED FROM THE LES.

consequently less NO. This is an important consideration to keep in mind for the design of ultra-low emissions system.

Some final consideration is given about the risk of flashback. Although flashback is not observed in the LES, the upstream propagation of the flame in the hydrogen blend case raises some concern about whether it could be triggered. While the upstream propagation is in fact mostly driven by the increased flame speed in the hydrogen blend and also its characteristic higher reaction rate at leaner conditions (resistance to lean extinction), the mixedness level near the centerline of the mixing tube also appears to be a critical factor as analysed earlier for Fig. 17. Indeed, this region is characterised by relatively high equivalence ratios and lower velocities, due to the presence of the recirculation bubble and the shear layers between inner axial air stream and swirling flow in the outer region of the mixing tube (see Fig. 15). Considering the presence of the PVC in the flow as discussed in Section 4.2, this situation can lead to a coupling between fluctuations of equivalence ratio, heat release and vorticity that can trigger flashback via the combustion induced vortex breakdown (CIVB) mechanism as for example discussed in [15, 16], with uncontrolled upstream propagation of the recirculation bubble. In such a case the amount of axial injection is not just to be designed to balance the higher flame speed of the hydrogen blend, but also to optimise the mixing process to avoid the aforementioned coupling to establish. It is worth to note that an increase in AAI also lead to increased pressure losses. This sensitivity to the amount of AAI and its effects on mixing and combustor efficiency will be therefore investigated in a future study. It is also worth to note that boundary layer flashback, which was neither observed or initiated in the present study, is in principle less likely at the operated conditions because of the high equivalence ratio near the wall caused by the fuel injection. Nevertheless, one should again be mindful that the recirculation bubble was observed to be still relatively far from the fuel injector ports in the present simulations. A possible further propagation upstream could result in the equivalence ratio near the wall crossing the flammability limits (which are very wide in the case of hydrogen) and triggering flashback via this mechanism rather than the CIVB mechanism. This aspect will also be investigated in a future study.

5. CONCLUSIONS

In the present work, the TU Delft swirl stabilized lean combustor was analysed at non-reacting and reacting conditions using a LES framework with thickened flame model and detailed chemical kinetics. Two fuels conditions are simulated, one consisting of 100% methane and the other having 16% split of hydrogen in mass and 86% methane. The two conditions are compared at the same power, implying that the equivalence ratio in the hydrogen blend case decreases from 0.75 to 0.7 to balance the higher reactivity of hydrogen in the fuel. A 5% of axial air injection is used in both conditions as a measure to prevent flashback. The methane-only case is simulated first and the results are compared with available PIV data. The predicted velocity field in the reacting case compares well with the experimental data in the region of the flame, while the results from the non-reacting case were found not to be directly comparable to those from the experiments due to some uncertainty in the boundary conditions. The presence of a PVC is further revealed through POD analysis for both reacting and non-reacting case, in agreement with the experiments.

The LES is then used to shed light on the effects of hydrogen addition. The PVC is still observed when hydrogen is added, but the associated modes appear to be suppressed near the combustor entrance. The highest temperature is also lower in the hydrogen blend case, which is a consequence of the lower global equivalence ratio and this is consistent with *a priori* flamelet computations. This is very beneficial in terms of emissions reduction, in particular NOx which is observed to decrease more than 70% in respect to the methane-only case. Nevertheless, the flame shifts significantly upstream in the case of the hydrogen blend and enters the mixing tube along with the recirculation bubble (most upstream part of the central recirculation zone). The higher flame speed of the hydrogen blend (despite the lower equivalence ratio) and its higher resistance to lean extinction are found to only partly explain this upstream propagation. An analysis of equivalence ratio distribution in the mixing tube reveals in fact that mixing is mostly driven by turbulent and molecular diffusion and this leads to a richer mixture near the centreline in the region immediately upstream the combustor entrance in the case of the hydrogen blend, due to the stronger diffusivity of the latter. Although flashback was not observed in the present work, these variations of equivalence ratio could couple with heat release and the vorticity generated by the recirculation bubble to trigger combustion induced vortex breakdown, for which the use of axial air injection might become ineffective. This should be taken

into account when designing new combustor geometries employing hydrogen or hydrogen blends. A careful balance between fuel port sizing, radial fuel momentum and axial air momentum needs to be designed when adding hydrogen to maintain the desired mixing characteristics. This interplay is the objective of a future study.

ACKNOWLEDGMENTS

This project has been financed by the Dutch Ministry of Economic Affairs and Climate under the TKI scheme (grant number TKI HTSM/18.0170) along with SAFRAN Tech and Airbus.

REFERENCES

[1] Noble, D., Wu, D., Emerson, B., Sheppard, S., Lieuwen, T. and Angello, L. "Assessment of current capabilities and near-term availability of hydrogen-fired gas turbines considering a low-carbon future." *J. Eng. Gas Turb. Power* Vol. 143 No. 4 (2021): p. 041002.

[2] Cho, E. S. and Chung, S. H. "Improvement of flame stability and NOx reduction in hydrogen-added ultra lean premixed combustion." *J. Mech. Sci. Technol.* Vol. 23 No. 3 (2009): pp. 650–658.

[3] Oztarlik, G., Selle, L., Poinsot, T. and Shuller, T. "Supression of instabilities of swirled premixed flames with minimal secondary hydrogen injection." *Combust. Flame* Vol. 214 (2020): pp. 266–276.

[4] Kiesewetter, F., Konle, M. and Sattelmayer, T. "Analysis of Combustion Induced Vortex Breakdown Driven Flame Flashback in a Premix Burner With Cylindrical Mixing Zone." *J. Eng. Gas Turbines Power* Vol. 129 (2007): pp. 929–936.

[5] Fric, T. F. "Effects of fuel-air unmixedness on NO(x) emissions." *J. Propul. Power* Vol. 9 (1993): pp. 708—-713.

[6] Baumgartner, G. and Sattelmayer, T. "Experimental Investigation on the Effect of Boundary Layer Fluid Injection on the Flashback Propensity of Premixed Hydrogen-Air Flames." *Proc. ASME Turbo Expo*. GT2013-94266. 2013.

[7] Reichel, T. G., Goeckeler, K. and Paschereit, C. O. "Investigation of lean premixed swirl-stabilized hydrogen burner with axial air injection using OH-PLIF imaging." *Proc. ASME Turbo Expo*. GT2015-4249. 2015.

[8] Burmberger, S. and Sattelmayer, T. "Optimization of the Aerodynamic Flame Stabilization for Fuel Flexible Gas Turbine Premix Burners." *J. Eng. Gas Turb. Power* Vol. 133 (2011): p. 101501.

[9] Reichel, Thoralf G, Terhaar, Steffen and Paschereit, Christian Oliver. "Flashback Resistance and Fuel–Air Mixing in Lean Premixed Hydrogen Combustion." *J. Propuls. Power* Vol. 34 No. 3 (2018): pp. 690–701.

[10] Reichel, T., S., Terhaar and Paschereit, C. O. "Increasing Flashback Resistance in Lean Premixed Swirl Stabilized Hydrogen Combustion by Axial Air Injection." *J. Eng. Gas Turbines Power* Vol. 137 (2015): p. 071503.

[11] Mayer, C., Sangl, J., Sattelmayer, T., Lachaux, T. and Bernero, S. "Study on the Operational Window of a Swirl Stabilized Syngas Burner Under Atmospheric and High Pressure Conditions." *J. Eng. Gas Turbines Power* Vol. 134 (2012): p. 031506.

[12] Sangl, J., Mayer, C. and Sattelmayer, T. "Dynamic Adaptation of Aerodynamic Flame Stabilization of a Premix Swirl Burner to Fuel Reactivity Using Fuel Momentum." *J. Eng. Gas Turbines Power* Vol. 133 (2011): p. 071501.

[13] Steinberg, A. M., Arndt, C. M. and Meier, W. "Parametric study of vortex structures and their dynamics in swirl-stabilized combustion." *Proc. Combust. Inst.* Vol. 34 (2013): pp. 3117–3125.

[14] Duwig, C. and Fuchs, L. "Study of flame stabilization in a swirling combustor using a new flamelet formulation." *Combust. Sci. Technol.* Vol. 177 (2007): pp. 1485–1510.

[15] Langella, I., Heinze, J., Behrendt, T., Voigt, L., Swaminathan, N. and Zedda, M. "Turbulent Flame Shape Switching at Conditions Relevant for Gas Turbines." *J. Eng. Gas Turbines Power* Vol. 142 No. 1 (2020).

[16] Soli, A. and Langella, I. "Numerical Investigation of a Coupled Blow-Off/Flashback Process in a High-Pressure Lean-Burn Combustor." *J. Eng. Gas Turbines Power* Vol. 145 (2022): p. 021010.

[17] Syred, N. "A review of oscillation mechanisms and the role of the precessing vortex core (PVC) in swirl combustion systems." *Prog. Energy Combust. Sci.* Vol. 32 (2006): pp. 93–161.

[18] Driscoll, J. F. and Temme, J. "Role of swirl in flame stabilization." *49th AIAA Aerospace Sciences Metting*. Orlando, Florida.

[19] van den Bergh, A. "Design and test of a swirl-stabilized methane combustor with axial air injection." Master's Thesis, Technical University of Delft. 2022.

[20] Veynante, D. and Vervisch, L. "Turbulent combustion modeling." *Prog. Energy Combust. Sci.* Vol. 28 No. 3 (2002): pp. 193–266.

[21] Colin, O., Ducros, F., Veynante, D. and Poinsot, T. J. "A thickened flame model for large eddy simulations of turbulent premixed combustion." *Phys. Fluids* Vol. 12 (2000): p. 1843.

[22] Warnatz, J., Maas, U., Dibble, R. W. and Warnatz, J. *Combustion*. Springer (2006).

[23] Eindhoven University of Technology. "CHEM1D. A one dimensional laminar flame code." (2021). URL https://github.com/thijsa93400/TUe_chem1d.

[24] Chumakov, S. G. and Rutland, C. J. "Dynamic structure subgrid-scale models for large eddy simulation." *Num Meth. Fluids* Vol. 47 No. 8 (2005): pp. 911–923.

[25] Chai, X. and Mahesh, K. "Dynamic k-Equation Model for Large Eddy Simulation of Compressible Flow." *J. Fluid Mech.* Vol. 699 (2012): pp. 385–413.

[26] Colin, O., Ducros, F., Veynante, D. and Poinsot, T. "A thickened flame model for large eddy simulations of turbulent premixed combustion." *Phys. Fluids* Vol. 12 No. 7 (2000): pp. 1843–1863.

[27] Frenklach, M., Wang, H., Goldenberg, M., Smith, G. P., Golden, D. M., Bowman, C. T., Hanson, R. K., Gardiner,

W. C. and Lissianski, V. "GRI-mech: An optimized detailed chemical reaction mechanism for methane combustion." Technical Report No. 199607. SRI International. 1995.

[28] Wang, G., Boileau, M. and Veynante, D. "Implementation of a dynamic thickened flame model for large eddy simulations of turbulent premixed combustion." *Combust. Flame* Vol. 158 (2011): pp. 2199–2213.

[29] Durand, L. and Polifke, W. "Implementation of the thickened flame model for large eddy simulation of turbulent premixed combustion in a commercial solver." *Turbo Expo: Power for Land, Sea, and Air*. GT2007-28188: pp. 869–878. 2007.

[30] Charlette, F., Meneveau, C. and Veynante, D. "A power-law flame wrinkling model for LES of premixed turbulent combustion, part II: dynamic formulation." *Combust. Flame* Vol. 131 (2002): pp. 181–197.

[31] Issa, R. I. "Solution of the implicitly discretised fluid flow equations by operator-splitting." *J. Comput. Phys.* Vol. 62 No. 1 (1986): pp. 40–65.

[32] Drennan, S. A. and Kumar, G. "Demonstration of an Automatic Meshing Approach for Simulation of a Liquid Fueled Gas Turbine with Detailed Chemistry." *50th AIAA/ASME/SAE/ASEE Joint Propulsion Conference*, Vol. 2014-3628. 2014.

[33] Werner, H. and Wengle, H. "Large-eddy simulation of turbulent flow over and around a cube in a plate channel." *Turbulent shear flows*. 8. Springer (1993): pp. 155–168.

[34] Bradshaw, P. and Huang, G. P. "The law of the wall in turbulent flow." *Proc. Royal Soc. London. Series A: Mathematical and Physical Sciences* Vol. 451 No. 1941 (1995): pp. 165–188.

[35] Pope, S. B. *Turbulent flows*. Cambridge University Press (2000).

[36] Germano, M., Piomelli, U., Moin, P. and Cabot, W. H. "A dynamic subgrid-scale eddy viscosity model." *Phys. Fluids A* Vol. 3 No. 7 (1991): p. 1760.

[37] Capurso, T, Laera, D, Riber, E and Cuenot, B. "NOx pathways in lean partially premixed swirling H2-air turbulent flame." *Combustion and Flame* Vol. 248 (2023): p. 112581.

[38] Chen, Zhi X, Langella, Ivan, Swaminathan, Nedunchezhian, Stöhr, Michael, Meier, Wolfgang and Kolla, Hemanth. "Large Eddy Simulation of a dual swirl gas turbine combustor: flame/flow structures and stabilisation under thermoacoustically stable and unstable conditions." *Combustion and Flame* Vol. 203 (2019): pp. 279–300.

[39] Massey, J. C., Chen, Z. X and Swaminathan, N. "Modelling Heat Loss Effects in the Large Eddy Simulation of a Lean Swirl-Stabilised Flame." *Flow Turbul. Combust.* Vol. 106 (2021): pp. 1355–1378.

[40] Sirovich, L. "Turbulence and the dynamics of coherent structures. I. Coherent structures." *Q. Appl. Math.* Vol. 45 No. 3 (1987): pp. 561–571.

[41] Oberleithner, K., Stöhr, M., Im, S. H., Arndt, C. M. and Steinberg, A. M. "Formation and flame-induced suppression of the precessing vortex core in a swirl combustor: experiments and linear stability analysis." *Combust. Flame* Vol. 162 No. 8 (2015): pp. 3100–3114.

[42] Dellenback, P. A., Metzger, D. E. and Neitzel, G. P. "Measurements in turbulent swirling flow through an abrupt axisymmetric expansion." *AIAA J.* Vol. 26 No. 6 (1988): pp. 669–681.

[43] Stöhr, M., Sadanandan, R. and Meier, W. "Phase-resolved characterization of vortex–flame interaction in a turbulent swirl flame." *Exp. Fluids* Vol. 51 No. 4 (2011): pp. 1153–1167.

[44] Beer, J. and Chigier, N. A. *Combustion Aerodynamics*. Krieger, Malabar, Fla. (1983).

[45] Choi, J., Jung, E., Kang, S. and Do, H. "Modeling swirl decay rate of turbulent flows in annular swirl injectors." *AIAA J.* Vol. 56 No. 12 (2018): pp. 4910–4926.

[46] Shahsavari, M., Farshchi, M. and Arabnejad, M. H. "Large eddy simulations of unconfined non-reacting and reacting turbulent low swirl jets." *Flow Turbul. Combust.* Vol. 98 No. 3 (2017): pp. 817–840.

[47] Huang, Y. and Yang, V. "Effect of swirl on combustion dynamics in a lean-premixed swirl-stabilized combustor." *Proc. Combust. Inst.* Vol. 30 No. 2 (2005): pp. 1775–1782.

[48] Dederichs, S., Zarzalis, N., Habisreuther, P., Beck, C., Prade, B. and Krebs, W. "Assessment of a gas turbine NOx reduction potential based on a spatiotemporal unmixedness parameter." *J. Eng. Gas Turbines Power* Vol. 135 No. 11 (2013).

[49] Li, H., ElKady, A. M. and Evulet, A. T. "Effect of exhaust gas recirculation on NOx formation in premixed combustion system." *47th AIAA Aerospace Sciences Meeting Including The New Horizons Forum and Aerospace Exposition*. 226. 2009.